Radio Frequency Interference Characterization and Mitigation for Polarimetric Weather Radar

A Study Case

Yin, Jiapeng; Hoogeboom, Peter; Unal, Christine; Russchenberg, Herman

DOI
10.1109/TGRS.2021.3093565

Publication date
2021

Document Version
Final published version

Published in
IEEE Transactions on Geoscience and Remote Sensing

Radio Frequency Interference Characterization and Mitigation for Polarimetric Weather Radar: A Study Case

Jiapeng Yin, Peter Hoogeboom, Christine Unal, and Herman Russchenberg

***Abstract*— Radio frequency interference (RFI) has become a growing concern for weather radar, distorting radar variable estimation. By simultaneously or alternately transmitting the horizontal and vertical polarized waves, polarimetric weather radar can be referred to as SHV radar or AHV radar. The SHV radar can mimic the AHV radar by discarding either H- or V-channel measurements, which leads to an alternating scheme. In this research, the real RFI measurements from an operational C-band SHV radar are used to characterize the RFI temporal, spectral, and polarimetric features. Then, the RFI is simulated to quantify the performance of the object-orientated spectral polarimetric (OBSPol) filter in RFI mitigation. The OBSPol filter has been previously proposed by the authors to mitigate the narrowband clutter (both stationary and moving) and noise. This work extends the application of the filter to remove the RFI for SHV radar. Specifically, by taking advantage of the low copolar correlation of the RFI signal measured in AHV radar, the RFI mitigation method is designed, and its effectiveness is proven by qualitative and quantitative analyses. In particular, in the case of RFI overlapped to weather echoes in the time domain, the RFI can be mitigated, also when the duty cycle of the RFI is high. However, this work does not provide a full evaluation of the RFI mitigation performance on all radar data outputs but a proof of concept to show the effectiveness of the proposed filter for RFI mitigation.**

***Index Terms*— Polarimetric weather radar, radio frequency interference (RFI), range-Doppler continuity, spectral polarimetric filter.**

I. Introduction

POLARIMETRIC Doppler weather radar is well recognized as an effective sensor for obtaining the microphysical and dynamical properties of precipitation at high spatial and temporal resolution [1]. The prerequisite of using weather radar data is sufficient measurement accuracy and precision. Apart from the radar system error that can be quantified by radar calibration technique [2], the primary error sources are different types of unwanted echoes termed clutter. The presence of various clutters may prevent detection of weather signals, change the weather signal statistics, or introduce bias on radar observables. Hence, it is important to design a multifunctional filter to mitigate all the clutter.

Nowadays, heavy demands for bandwidth in the radio frequency (RF) spectrum force its shared use. There is a growing concern about the effects of unwanted RF signals in weather radars [3]. For example, band 5470–5720 MHz was assigned to the mobile service for the operation of wireless access systems, including radio local area networks (RLANs) at the World Radio-communication Conference 2003 [4]. The allocated bands partially overlap with the bands used by existing C-band radars, which may introduce some RF interference (RFI).

The coexistence of weather radar with RLAN requires the dynamic frequency selection (DFS) equipment in RLAN systems to detect radar signals [5]. Before using a channel, a check for the presence of radar signals for a time period initially set to 60 s is carried out by the DFS, and the decision should be made in RLAN to avoid the frequencies in use by radars. However, some DFS only consider "simple" radar characteristics, such as pulse widths over 1 μs and a fixed pulse repetition interval [6]. This makes DFS unreliable in avoiding RFI in radar systems.

In the past 15 years, the reported RFI contamination issues on C-band weather radars have been increasing [5]. Typical examples are the Terminal Doppler Weather Radar (TDWR) [7] and the European National Meteorological Services Network (EUMETNET) [8]. Moreover, there is an increasing number of cases from S-band radars (e.g., the National Weather Service Weather Radar termed NEXRAD), which are caused by adjacent band interference from wireless networks and in-band interference from other government radars [8].

Hence, the detection and mitigation of RFI at the radar signal processing level are in high demand. The signatures of RFI on radar plan position indicator (PPI) are dots, spokes, or stripes [8], which contaminates large portions of a weather radar scanning volume. By comparing the amplitude of each pulse to that of its immediate neighbors or the median over the dwell time, the 1-D median RFI filter [9] and

Manuscript received December 9, 2020; revised March 23, 2021 and May 23, 2021; accepted June 13, 2021. The work of Jiapeng Yin was supported in part by the Postdoctoral International Exchange Program under Grant 48132 and in part by the Science and Technology Innovation Program of Hunan Province under Grant 2020RC2042. *(Corresponding author: Jiapeng Yin.)*

Jiapeng Yin is with the College of Electronic Science, National University of Defense Technology, Changsha 410073, China (e-mail: jiapeng.yin@hotmail.com).

Peter Hoogeboom, Christine Unal, and Herman Russchenberg are with the Department of Geoscience and Remote Sensing, Delft University of Technology, 2628 CN Delft, The Netherlands (e-mail: p.hoogeboom@tudelft.nl; c.m.h.unal@tudelft.nl; h.w.j.russchenberg@tudelft.nl).

Digital Object Identifier 10.1109/TGRS.2021.3093565

Vaisala-3 RFI filter [10] were proposed. However, the RFI cannot be completely removed by these two filters. Based on the amplitude-anomaly property of RFI in the range-time domain, a 2-D RFI filter was designed [3], which shows better performance in RFI removal compared with the aforementioned methods.

However, these time-domain methods are especially suitable for low to medium duty cycle interference (less than 10% [3]). When the duty cycle of the interferer surpasses 50%, which means that, in the time domain, not enough clean data are left for data processing, Doppler spectral filtering is recommended [3]. Moreover, the removal in the time domain has, for a case of weak signals and strong interference, the risk of removing or reducing the atmospheric signal.

To cope with the problems of the time-domain method, filters in the Doppler domain can be considered. In the Doppler domain, RFI in weather radars presents as raised noise [11]. If the weather signal is not completely covered by the raised noise floor, the weather observables can be recovered. A spectral polarimetric filter based on a fuzzy-logic classification algorithm was proposed [12], but its performance in RFI mitigation was not fully discussed.

To mitigate the RF signatures and alleviate the problem of high duty cycle RFI, a spectral polarimetric filter named the object-orientated spectral polarimetric (OBSPol) filter [13] is investigated in this article. The OBSPol filter is a multifunctional filter, which can simultaneously remove various types of clutter. Specifically, it was initially put forward to mitigate narrowband clutter (i.e., moving clutter and ground clutter) and is now analyzed for removing the RFI. Taking advantage of the spectral polarimetric features and range-Doppler continuity of precipitation, the filter is implemented in the range-Doppler spectrogram (i.e., one ray in radar PPI) to mitigate the clutter. The filter will generate a filtering mask that is applied to the raw range-Doppler spectrogram to retain the precipitation and remove the clutter. The filter can be used in polarimetric weather radar without cross-polar measurements.

Raw data examples from a C-band pulse-Doppler radar contaminated by RFI are analyzed. We first characterize the features of the RFI in the temporal and spectral domain using the real radar measurements and then use the obtained features to simulate the situation where the dual-polarization radar is contaminated by RFI to quantify the performance of the spectral polarimetric filter.

The structure of this article is given as follows. Based on RFI contaminated weather radar data, RFI characterization is given in Section II for single-polarization and polarimetric radar. The RFI model and simulation in weather radar are introduced in Section III. Section IV discusses the OBSPol filter and its applications in RFI mitigation. Finally, Section V draws conclusions.

II. RFI Characterization

A. RFI-Contaminated Weather Radar Data

Characterization of RFI is required to enhance the mitigating filtering procedures. In this article, RFI simulation is used based on the properties of real RFI. The data are taken from the weather radar systems of the Royal Netherlands Meteorological Institute (referred to as KNMI, taken from the Dutch abbreviation). From May 12, 2017, KNMI operated new weather radar systems, upgrading from single-polarization (i.e., Selex Meteor 360) to dual-polarization (i.e., Selex Meteor 735CDP10). The two new radars located at Herwijnen and Den Helder can cover the whole Netherlands. The radars are also part of the EUMETNET [14]. The KNMI radars have 16 scanning modes with different configurations sequentially performed in 5-min observation interval. A precipitation map is compiled for the public and weather forecast [15]. In addition, all the processed radar data are freely accessible online [16]. The specifications of the KNMI radars are shown in Table I.

TABLE I
KNMI Radar Specifications

Radar type	Pulsed Doppler
Transmitter type	Magnetron
Polarization	Dual-polarization
Center frequency (GHz)	5.633(Herwijnen), 5.625(Den Helder)
Transmitted power (kW)	500
Pulse width (μs)	0.5 - 3.5
Pulse repetition frequency (Hz)	175 - 2400
Antenna beamwidth	$\leq 1^\circ$
Operational angles	Elevation -2° - 90°, Azimuth 0° - 360°
Scanning strategy	16 modes in 5 minutes

To analyze the features of the RFI, some I/Q data were recorded. Data collected at 17:17 UTC on October 26, 2017, are shown in Fig. 1(a). The data were measured in the configuration as follows: the antenna speed was 2 rpm, the elevation angle was 0.3°, the pulse repetition frequency was 449 Hz, and the range resolution was 0.4 km.

In the PPI of Fig. 1(a), the RFI shows spikes along with the whole range in some azimuth directions. Some of these RFI overlap with the precipitation. The RFI pulses are not synchronized with the radar timing; therefore, they occur randomly with approximately equal signal strength at a large number of ranges in the dwell time, whereas the strength of atmospheric signals is range-dependent.

The standard processing of KNMI radar consists of an IIR, DFT linear, or Gaussian iterative interpolation, which is incapable of RFI signature mitigation. Hence, it is imperative to find a solution that can be implemented in real time to mitigate the RFI.

First, it will be shown that the Doppler power spectra of the measured RFI resemble as raised noise, as concluded in [11]. Next, in the analysis of RFI filtering for polarimetric radar, similar noise signals will be injected to study the filtering merits in a controlled fashion.

B. RFI Characterization in Single Polarization Radar

To analyze the features of the RFI, some data are taken and displayed in both time and Doppler domains. Ray 70, as is labeled in Fig. 1(a), is considered as an example of the RFI contamination. The ray numbers of the raw data are labeled in the order of time series, in this case, 226 rays for one clockwise antenna rotation, with arbitrary starting azimuth angle. The ray numbers may vary in different elevation angles due to different measurement requirements.

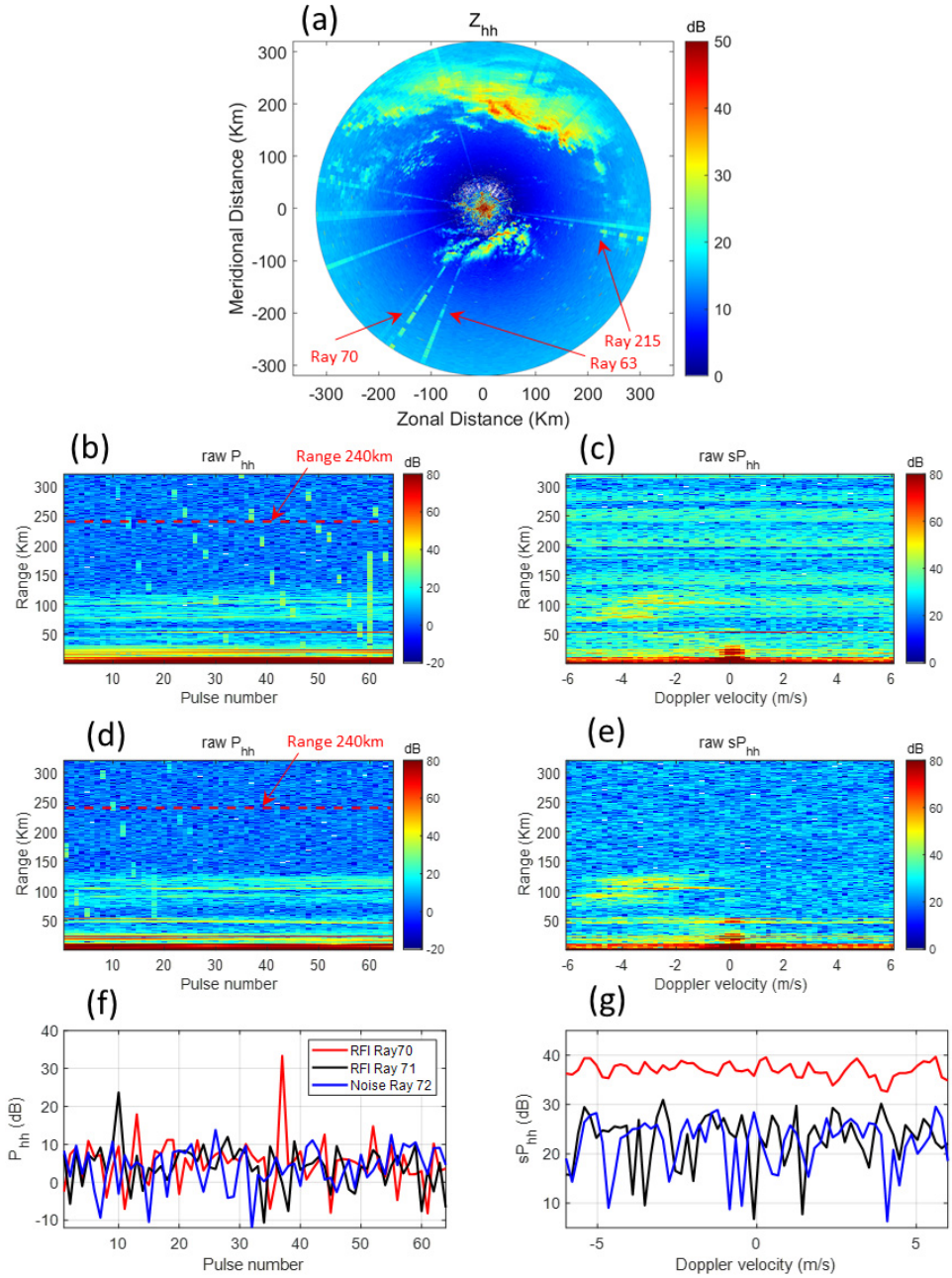

Fig. 1. KNMI Herwijnen radar measurements. (a) Raw PPI of Z_{hh}; (b) range-time image of Ray 70; (c) range-Doppler spectrogram of Ray 70; (d) range-time image of Ray 71; (e) range-Doppler spectrogram of Ray 71; (f) backscattered power of RFI and noise versus pulse number at range 240 km; and (g) power spectra of RFI and noise versus Doppler velocity at range 240 km.

Fig. 1(b) shows the backscattered power versus range (i.e., fast time) and pulse number (i.e., slow time). Irregularly positioned short spikes can be observed. Since the RFI pulses are not synchronized with the radar timing, the appearance of RFI depends on the RFI duty cycle and the rotating speed of the radar antenna.

For the Doppler processing, the number of pulses in the Fourier transform window is set to be 64, which corresponds to a Doppler velocity resolution of 18.8 cm s^{-1}, and an azimuth resolution of 1.6°. A Hamming window is applied to suppress spectral leakage. A range-Doppler spectrogram is obtained [see Fig. 1(c)] when the Fourier transform is applied on the received signal along with the time domain (i.e., the pulses) for each range. We can see that the precipitation is heavily masked by the interference. A single RFI spike in the time domain introduces a wide noise-like response in the Doppler domain, just as may be expected in theory from the Fourier transform of a Dirac pulse.

In addition, Ray 71 is inspected, and its range-time image and range-Doppler spectrogram are shown in Fig. 1(d) and (e). The first 30 pulses of the range-time image of Ray 71 have spikes similar to that of Ray 70, while the rest has no spikes and is, therefore, free of RFI contamination.

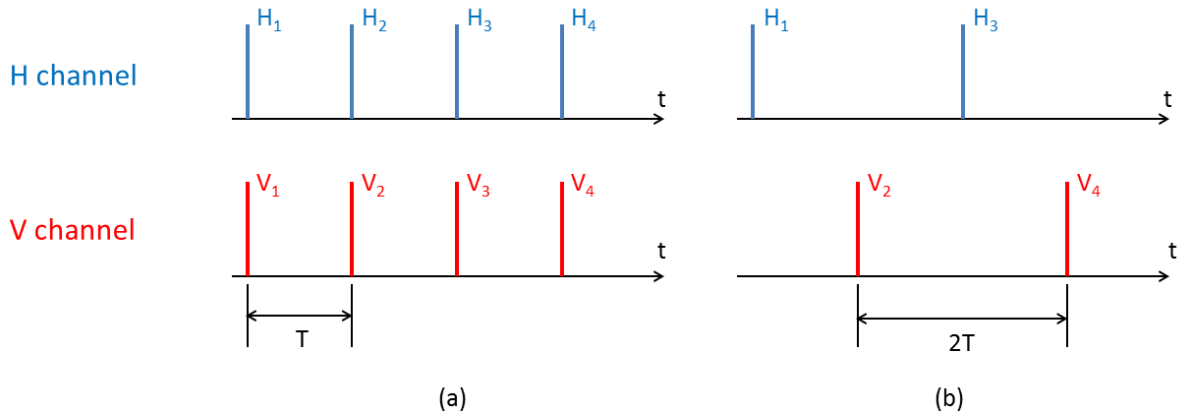

Fig. 2. Schematic of pulse sequences [17]. (a) SHV mode. (b) AHV mode.

Fig. 1(f) and (g) shows the time-domain power and the Doppler spectrum of a single range bin at 240 km. Rays 70, 71, and 72 are displayed. The strong spike in the time domain of Ray 70 leads to a high level of interference in the spectral domain, thereby masking the thermal noise, whereas Ray 72, which contains no RFI, shows the thermal noise only. It is clear that, in the spectral domain, the RFI signal is noise-like, albeit that the variance is much smaller than the one for noise. Still, the bandwidth of RFI signals is much wider than the bandwidth of weather radars, and thereby, it contributes to the noisy character of RFI as experienced in weather radar Doppler spectra.

The interference-to-noise ratio (INR) parameter is introduced here to enable realistic and comparable interference levels in simulations. This allows for a better performance quantification of the RFI filter. According to the study case in Fig. 1, a maximum INR of about 20 dB in the time domain is observed.

In conclusion, the above observations support the approximation of RFI as a raised noise level in the spectral domain, as was also concluded in [3]. This behavior characterizes the RFI type RLAN.

C. RFI Characterization in Polarimetric Radar

1) Polarimetric Radar Types and RFI: Currently, most polarimetric weather radars are designed to use linear polarizations as the polarization basis. Generally, these radars are equipped with a dual-channel receiver, one horizontal polarized, and one vertical polarized, while an RFI signal can have arbitrary polarization, either linear or circular [18]. In this sense, RFI sensed by radar with a linear polarization basis will be decomposed into horizontal and vertical polarization components.

Consequently, when we operate a linearly polarized radar with a circularly polarized interferer, the situation will resemble the 45° linear polarized RFI case. The circular polarization signal will generate equal strength signals in both the horizontal and vertical channels. There is a phase difference but in the power measures, which will not be noticed.

In summary, a linear polarization (not strictly H or V) or a circular polarization will be decomposed by the receive channels into horizontal and vertical components. In general, these components will have different amplitudes (except for a 45° linearly polarized signal and a perfect circular polarized one) but show a strong correlation. For circular polarization, a 90° phase shift will occur between the V- and H-channels, but this has no impact on the copolar correlation coefficient estimation.

The received signals in the polarimetric radar are linked to the polarization of the transmitted pulse by a 2×2 complex scattering matrix S

$$S = \begin{bmatrix} S_{hh} & S_{hv} \\ S_{vh} & S_{vv} \end{bmatrix} \tag{1}$$

where S_{xy} is a complex scattering matrix component with a transmitted y polarization and a received x polarization, with x and y being horizontal polarization (i.e., h) or vertical polarization (i.e., v). In the case of backscattering in a reciprocal medium (e.g., precipitation), $S_{hv} = S_{vh}$.

A distinction has to be made based on the transmit pulse sequences. Polarimetric radars can be divided into two types: 1) simultaneous transmission of horizontally and vertically polarized waves (SHV mode) and 2) alternate transmission of horizontally and vertically polarized waves (AHV mode). The schematic is displayed in Fig. 2 [17].

Most operational polarimetric weather radars operate in the SHV mode and do not produce cross-polar measurements. RFI signals in the HH- and VV-channels will show a correlation in this case, unless it is horizontally or vertically polarized. However, in the AHV mode, the HH component is measured at a different time than the VV component, and therefore, the RFI measured components will be uncorrelated.

Compared with the SHV mode, the AHV mode has the advantage of straightforward measurement of the cross-polar backscattering. In this case, RFI simultaneously received in the copolar and cross-polar channels will have its components correlated. A drawback of AHV mode is the reduction of the maximum unambiguous Doppler velocity. This can be compensated for by advanced techniques [19]. Polarimetric radar in AHV mode is also referred to as full-polarimetric weather radar. The dependence of RFI on the radar receiver has also been discussed in [20].

In this article, the RFI mitigation for polarimetric radar in the SHV mode will be discussed using the KNMI C-band radars. To quantify the effectiveness of the spectral polarimetric filter, simulated RFI will also be added to KNMI radar data.

2) Polarimetric Observables: Before analyzing RFI effects, some polarimetric observables that will be used in the filter are introduced. First, following the backscatter alignment convention, the reflectivity that relates to the range r is defined as

$$Z_{xy}(r) = C \cdot P_{xy}(r) \cdot r^2 = C \cdot \left|S_{xy}(r)\right|^2 \cdot r^2 \tag{2}$$

where $P_{xy}(r)$ is the backscattered power at range r with a transmitted y polarization and a received x polarization, and C is the calibration constant. Correspondingly, the well-known polarimetric observables, such as the differential reflectivity Z_{dr} and the copolar correlation coefficient ρ_{co}, can be defined as

$$Z_{\mathrm{dr}}(r) = \frac{Z_{hh}(r)}{Z_{vv}(r)} \tag{3}$$

$$\rho_{\mathrm{co}}(r) = \frac{\left|\left\langle S_{hh}(r) S_{vv}^{*}(r)\right\rangle\right|}{\sqrt{\left\langle |S_{hh}(r)|^2\right\rangle \left\langle |S_{vv}(r)|^2\right\rangle}} \tag{4}$$

where $\langle\rangle$ in ρ_{co} represents the averaging and $*$ is the complex conjugate.

Based on the combined simultaneous Doppler and polarization information, spectral polarimetry can help reveal the microphysical and dynamical properties of weather radar targets. This is favorable for retrieval of atmospheric microphysical information and mitigation of nonatmospheric echoes at the same time. The spectral reflectivity that relates to range r and Doppler velocity v is expressed as

$$sZ_{xy}(r, v) = C \cdot sP_{xy}(r, v) \cdot r^2 = C \cdot \left|sS_{xy}(r, v)\right|^2 \cdot r^2 \tag{5}$$

where $sS_{xy}(r, v)$ represents the complex Doppler velocity spectrum and $sP_{xy}(r, v)$ is defined as spectral power. Correspondingly, we can define the spectral differential reflectivity sZ_{dr} and the spectral copolar correlation coefficient $s\rho_{\mathrm{co}}$ as

$$sZ_{\mathrm{dr}}(r, v) = \frac{sZ_{hh}(r, v)}{sZ_{vv}(r, v)} \tag{6}$$

$$s\rho_{\mathrm{co}}(r, v) = \frac{\left|\left\langle S_{hh}(r, v) S_{vv}^{*}(r, v)\right\rangle\right|}{\sqrt{\left\langle |S_{hh}(r, v)|^2\right\rangle \left\langle |S_{vv}(r, v)|^2\right\rangle}} \tag{7}$$

where $\langle\rangle$ in $s\rho_{\mathrm{co}}$ represents the averaging either in range or Doppler, with the latter being chosen in this article.

After spectral polarimetric filtering, the bins retained in the Doppler domain are regarded as atmospheric signals. Then, better noise-free standard observables can be estimated. For example, the reflectivity at the range r is expressed as

$$Z_{hh}(r) = C \cdot \sum_{v \in atm} (sP_{hh}(r, v) - sN) \cdot r^2 \tag{8}$$

where $v \in atm$ signifies that only those Doppler bins that contain atmospheric signals are used, and sN is the spectral noise for the chosen spectrogram. The spectral noise is estimated from a histogram of sP_{hh} compiled across r and v. The most occurring bin value is regarded as the estimated spectral noise. The spectrogram-by-spectrogram noise estimation is inspired by Ivić *et al.* [21], which is proposed to accurately produce estimates of the system noise power. Note that sN is estimated based on a whole spectrogram; thus, it is independent of range.

TABLE II

POLARIMETRIC FEATURES OF RFI VERSUS DIFFERENT RF POLARIZATIONS

variable \ RF pol	H pol	45° pol	V pol
$Z_{dr}(dB)$	inf	0	-inf
ρ_{co} in SHV mode	small	large	small
ρ_{co} in AHV mode	small		

3) Polarimetric Signature of RFI and Precipitation: The measured polarimetric signature of RFI depends on the polarization of the RFI transmission. Also, the weather radar mode, SHV or AHV, leads to a different signature. Furthermore, in spectral polarimetric observables, the RFI will be more or less uniformly distributed over all spectral bins due to its noise-like properties, as discussed in Section II-B. Since atmospheric signals will always be contained in a part of the spectral bins, the filtering based on spectral polarimetric observables will lead to substantial improvement for RFI suppression in a similar fashion as thermal noise and clutter can be suppressed in these observables. The boundaries of the polarimetric signature of linear polarized RFI are expressed in Table II. As stated earlier, the polarimetric features of circular and 45° linear polarized RFI are similar.

The dB values of Z_{dr} will change from positive to negative when RF polarization gradually varies from horizontal to vertical. Z_{dr} values of liquid precipitation concentrate around 0 dB (light rain) or are positive. This means that it is difficult to distinguish RFI from liquid precipitation by using only Z_{dr} thresholding.

ρ_{co} is the phase-sensitive; consequently, the expression of RFI differs according to the polarimetric radar mode. For the SHV mode, linear polarized RFI will go into horizontal and vertical channels simultaneously; thus, the strong correlation of RFI in the two channels will result in large ρ_{co} values, unless RFI is horizontally or vertically polarized. On the other hand, ρ_{co} values of RFI are small in the AHV mode. Due to the time delay between horizontal and vertical channels, different RFI pulses are received in the two channels. For precipitation, the coherence time is long enough to maintain large ρ_{co} values for both SHV and AHV modes. This provides a powerful way to mitigate RFI, suitable for both AHV and SHV modes radars, as will be shown later on.

In summary, RFI has a noise-like signature in the spectral domain. However, its polarimetric signature differs from the noise one, which makes RFI a pseudonoise. Having built the polarimetric model of linear polarized RFI type RLAN, we analyze next the measured polarimetric signature of RFI based on the KNMI radar data.

4) Practical Analysis of Spectral Polarimetric Features in SHV Radar: Spectral polarimetric observables are analyzed in this part because of their better capabilities in RFI filtering.

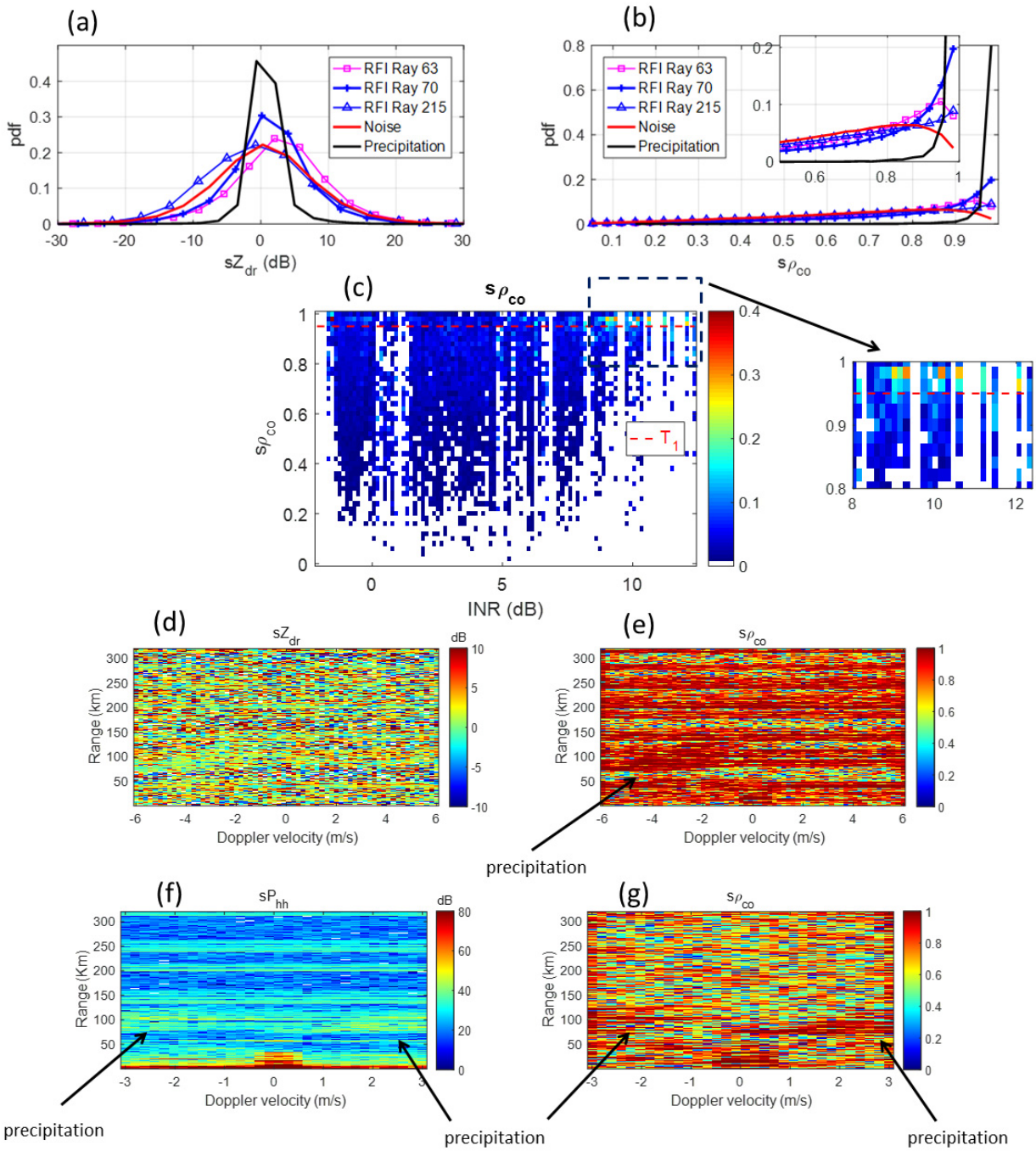

Fig. 3. Spectral polarimetric variables of RFI in KNMI Herwijnen radar data. (a) Experimental pdfs of sZ_{dr}; (b) experimental pdfs of $s\rho_{co}$; (c) $s\rho_{co}$ distribution versus INR; (d) sZ_{dr} spectrogram in the SHV mode; (e) $s\rho_{co}$ spectrogram in the SHV mode; (f) sP_{hh} spectrogram in the AHV mode; and (g) $s\rho_{co}$ spectrogram in the AHV mode.

Data from the KNMI Herwijnen SHV radar are displayed in Fig. 1(a). Specifically, Ray 63, Ray 70, and Ray 215 are chosen as data with RFI contamination. All the spectral bins of the rays with RFI in the range interval between 140 and 320 km are taken. The chosen areas cover RFI with different INR values, including noise-only bins. Experimental pdfs of spectral polarimetric observables of noise only and liquid precipitation are given for comparison. They are displayed in Fig. 3(a) and (b). Note that the experimental pdfs of typical polarimetric variables, namely, reflectivity and differential reflectivity, are provided in the literature [5] and share a similar distribution tendency with the spectral ones that are discussed in detail next.

The spectral differential reflectivity sZ_{dr} is a shape indicator of hydrometeors, and it has been investigated for clutter suppression to separate bird and insect echoes for wind retrievals [22]. As shown in Fig. 3(a), the sZ_{dr} value distribution of RFI varies from ray to ray, having positive, negative or zero mean values. Pure noise has a zero mean sZ_{dr} value. The sZ_{dr} values of both RFI and noise are broadly distributed in the

interval of [−20 dB, 20 dB], while that of liquid precipitation concentrates on [−3 dB, 4 dB]. In this case, all the sZ_{dr} values of RFI have a near-zero mean, indicating that the RFI has a polarization of approximately 45°. One example of sZ_{dr} from Ray 70 is shown in Fig. 3(d). The overlapping values make it difficult if not impossible to distinguish precipitation buried in noise and/or RFI using thresholding techniques.

The spectral copolar correlation coefficient $s\rho_{\mathrm{co}}$, which is available for most polarimetric radar systems, has been used as an efficient classification observable [23]. One key feature of $s\rho_{\mathrm{co}}$ is that its value is very close to 1 for most hydrometeors and significantly lower than 1 for nonmeteorological scatterers measured in the sidelobes of the antenna pattern. The $s\rho_{\mathrm{co}}$ values of the KNMI Herwijnen radar are calculated using a running average on 3 consecutive Doppler bins. As discussed in Section II-C, for RFI with arbitrary polarization (not strictly H or V), high values near 1 are expected in SHV mode. Indeed, in Fig. 3(b), high values of $s\rho_{\mathrm{co}}$ are found for some RFI bins. The pdf indicates that 8%–20% of the RFI data have high $s\rho_{\mathrm{co}}$ values larger than 0.95. The bins with lower values contain also noise, as is indicated by the INR. When INR is low, the spectral polarimetric features of RFI and noise tend to be the same. Ray 70 has the largest INR, followed by Ray 63 and then Ray 215. This is consistent with the pdf of the $s\rho_{\mathrm{co}}$ values close to 1 [see the zoomed-in part in Fig. 3(b)].

To further explore the influence of INR on $s\rho_{\mathrm{co}}$ values, we display the same $s\rho_{\mathrm{co}}$ data versus INR and normalize the frequency of $s\rho_{\mathrm{co}}$ values in each INR bin, as shown in Fig. 3(c). We observe that, when the INR is less than 5 dB, $s\rho_{\mathrm{co}}$ values are broadly distributed in the interval of [0, 1]. As INR increases, the $s\rho_{\mathrm{co}}$ values tend to concentrate to 1, with most values greater than 0.95. In addition, one example of $s\rho_{\mathrm{co}}$ from Ray 70 (the ray with the largest INR) is shown in Fig. 3(e). The precipitation, which is almost masked by RFI, is located in the range of 100–150 km at the negative Doppler velocity side.

RFI suppression in SHV radar can be achieved if correlated pulses are removed for the $s\rho_{\mathrm{co}}$ estimation. Thus, from each set of simultaneously measured H- and V-polarizations, either the H- or V-channel is discarded, in an alternating scheme. Specifically, data of H_{2m-1} and V_{2m} (or H_{2m} and V_{2m-1}) in Fig. 2(a) are used, where $m = 1, 2, \ldots, M/2$ and M is the total number of samples in the dwell time. The resulting datastream resembles an AHV radar one. Taking the H_{2m-1} samples, the spectral power sP_{hh} is generated, as displayed in Fig. 3(f). Bins with values less than 0 dB are displayed in white. Combined with V_{2m} samples, we have the $s\rho_{\mathrm{co}}$ spectrogram, as shown in Fig. 3(g), in which the polarimetric correlation of RFI has significantly decreased, but that of precipitation stands out. Implementing the spectral polarimetric filters based on Fig. 3(g) preserves the precipitation and removes the RFI, providing a way to mitigate the RFI in SHV radar.

A disadvantage of this method is the decrease in maximum unambiguous Doppler velocity by a factor of 2 because the time between two consecutive samples is doubled, resulting in Doppler aliasing. The precipitation is now mainly located in the area of positive Doppler velocities. However, this problem is well-known from AHV mode radars, and correction methods have been published [19].

The considered PPI measurement is meant to provide reflectivity measurements having a large maximum range (334 km) at the cost of the maximum unambiguous Doppler velocity. With the proposed methodology, reflectivity measurements severely contaminated by RFI can be improved. However, increasing the pulse repetition interval may lead to the violation of the coherency criterion for velocity estimation in such a case where the initial maximum unambiguous Doppler velocity is small. Generally, for the estimation of Doppler measurements, another measurement configuration is selected.

To conclude, on the one hand, RFI in polarimetric radar can be regarded as raised noise in the spectral domain for each channel (also applied to single-polarization radar). On the other hand, considering the correlation between two channels, different polarimetric radar types have different impacts. For SHV radar, the RFI sensed by the horizontal and vertical channels will be correlated. This correlation will increase with the INR, while, for AHV radar, RFI detected by the two consecutive channels will be uncorrelated. The correlation or noncorrelation of the polarimetric signals is the important point in this work.

The RFI type RLAN simulation in Section III where the RFI is 45° polarized follows these assumptions. In Section IV-B, the simulation will be extended to different linear polarizations. The RFI model is selected as a proof of concept for spectral polarimetric filtering.

III. RFI Model and Simulation in Weather Radar

A. Simulated RFI in Single Polarization Radar

For simulation of RFI, it is important to know the approximate RFI signal level that may be expected. For various reasons, it may be different from one radar to another. However, if the RFI level is expressed in terms of the radar's thermal noise, it can be transferred to other radars and lead to comparative results in RFI mitigation because the designed filters operate on the noise in radar data. Thus, for a given radar, the mitigation that can be expected follows from a measurement of the INR, and from comparison with the result, in this article.

The weather radar equation in the presence of noise and RFI is first derived. Rewriting (2) to express the reflectivity, we have

$$Z_{hh} = C \cdot P_{hh} \cdot r^2. \tag{9}$$

In the presence of RFI, P_{hh} will contain thermal noise and RFI. As mentioned in Section II-B, RFI can be simulated by noise in the spectral domain. The received power, P_{hh}, results from the integration of the spectral power. Thus, we define the total noise N_{tot} in P_{hh} as

$$N_{\mathrm{tot}} = N_{th} + N_{\mathrm{RFI}} = N_{th}(1 + \mathrm{INR}) \tag{10}$$

where N_{th} is the estimated thermal noise, N_{RFI} is the RFI power, and the INR is defined as

$$\mathrm{INR} = \frac{N_{\mathrm{RFI}}}{N_{th}}. \tag{11}$$

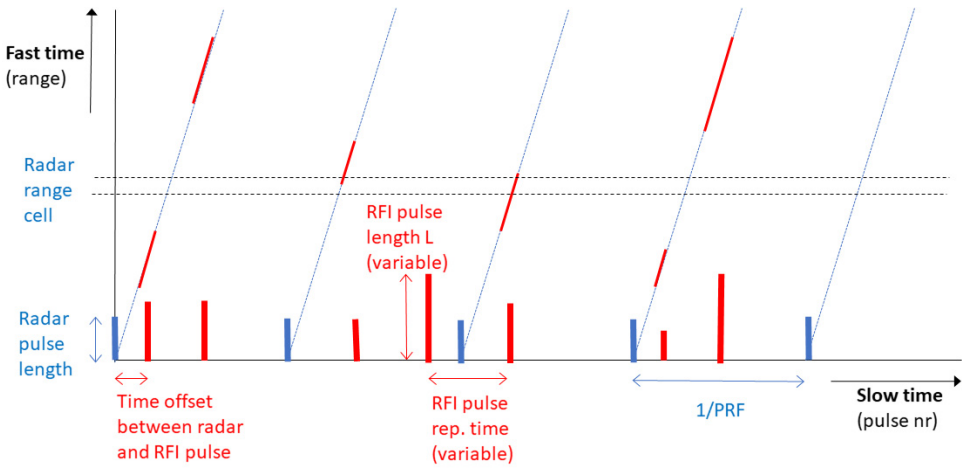

Fig. 4. Scheme diagram of simulated RFI pattern in the time domain.

The noise equivalent reflectivity Z_{noise} is the value where P_{hh} equals N_{th}. This is the smallest reflectivity value that can be measured by radar, and it is range-dependent, as shown in Fig. 1(a). In the case of RFI, Z_{noise} is increased because of the additional power N_{RFI}.

The INR of the KNMI Herwijnen data can be measured by comparing the RFI-contaminated reflectivity Z_{hh}^{RFI} with noise equivalent reflectivity Z_{noise} in the PPI as

$$\text{INR}(r) = \frac{Z_{hh}^{\text{RFI}}(r) - Z_{\text{noise}}(r)}{Z_{\text{noise}}(r)}. \tag{12}$$

INR has been introduced to have a parameter that does not depend too much on the weather radar itself. This makes a comparison to other radars much easier. INR depends mainly on the interferer transmit power, antenna gain, antenna pointing direction, and, most importantly, the propagation path from the interferer to the radar. One should expect a wider INR range in general. Considering the KNMI Herwijnen data in Fig. 1(a), the calculated maximum INR is 20.8dB. Thus, the INR ranging from 15 to 25 dB is used to study the performance of RFI filters in the simulation.

A simple model is derived from the characterization of the RFI of the study case in Section II. The schematic diagram of the RFI model in the time domain is shown in Fig. 4, where the x-axis is a slow time and the y-axis is a fast time. The blue pulses are the radar transmitted pulses, and the red ones are the received RFI by the radar. Two parameters, namely, RFI pulselength L_{RFI} and RFI pulse repetition time T_{RFI}, will control the RFI pattern. Specifically, the RFI pulselength L_{RFI} can be defined as

$$L_{\text{RFI}} = l \cdot \Delta R \tag{13}$$

where l is an integer and ΔR is the radar range resolution. Correspondingly, we define $\Delta t = \Delta R/2c$, where c is the velocity of light. Then, the RFI pulse repetition time T_{RFI} can be defined as

$$T_{\text{RFI}} = n \cdot T_0 + m \cdot \Delta t \tag{14}$$

where n and m are integers, and T_0 is the pulse repetition time.

Different combinations of L_{RFI} and T_{RFI} will result in different RFI patterns. The length, L_{RFI}, may correspond to several contiguous range bins, and T_{RFI} makes the RFI sparse or dense. Equations (13) and (14) are based on a general mathematic model built for the RFI parameters, which can be irregular if the parameters change quickly. It is not necessarily limited to regular pulse patterns. However, the regularity or nonregularity of the RFI patterns in the time domain does not impact the filter in the spectral domain.

In addition, a ratio of the RFI-contaminated bins to the total number of bins in the range-pulse image, termed the RFI contamination ratio, can be defined to quantify the severity of RFI contamination. Fig. 1(b) and (d) shows the typical cases where the RFI contamination ratio is small. However, when the RFI contamination ratio is large, as mentioned in the introduction, the time-domain methods will not work in mitigating the RFI.

In the simulation, the INR of the simulated RFI can be calculated in the spectral domain for each range bin, as indicated in (12). As mentioned in the literature [3], the RFI powers follow exponential distributions (or, equivalently, Rayleigh distributions for the amplitudes), which will also be used for the simulation in this work. Since the INR is dependent on the RFI pattern and the signal-to-noise ratio (SNR) of the individual RFI pulses in the dwell time, a given INR for each simulation cannot be predefined. However, by fixing the RFI pattern and tuning the parameters of the Rayleigh distributions of the RFI amplitudes in the dwell time, we can get the INR close to what we expect. For SHV radar, the RFI pattern can be applied in two channels without any adjustment.

B. Simulated RFI in SHV Radar

The RFI simulation uses the KNMI radar data. To simulate the situation where SHV radar is contaminated by RFI, pulse-like noise with different SNRs can be added to the KNMI data. RFI pulses with the maximum SNR of 30 dB are added to Rays 84, 120, and 160 of the KNMI Herwijnen data shown in Fig. 1. The simulated result is displayed in Fig. 5(b). The RFI is clearly visible along with the whole range in

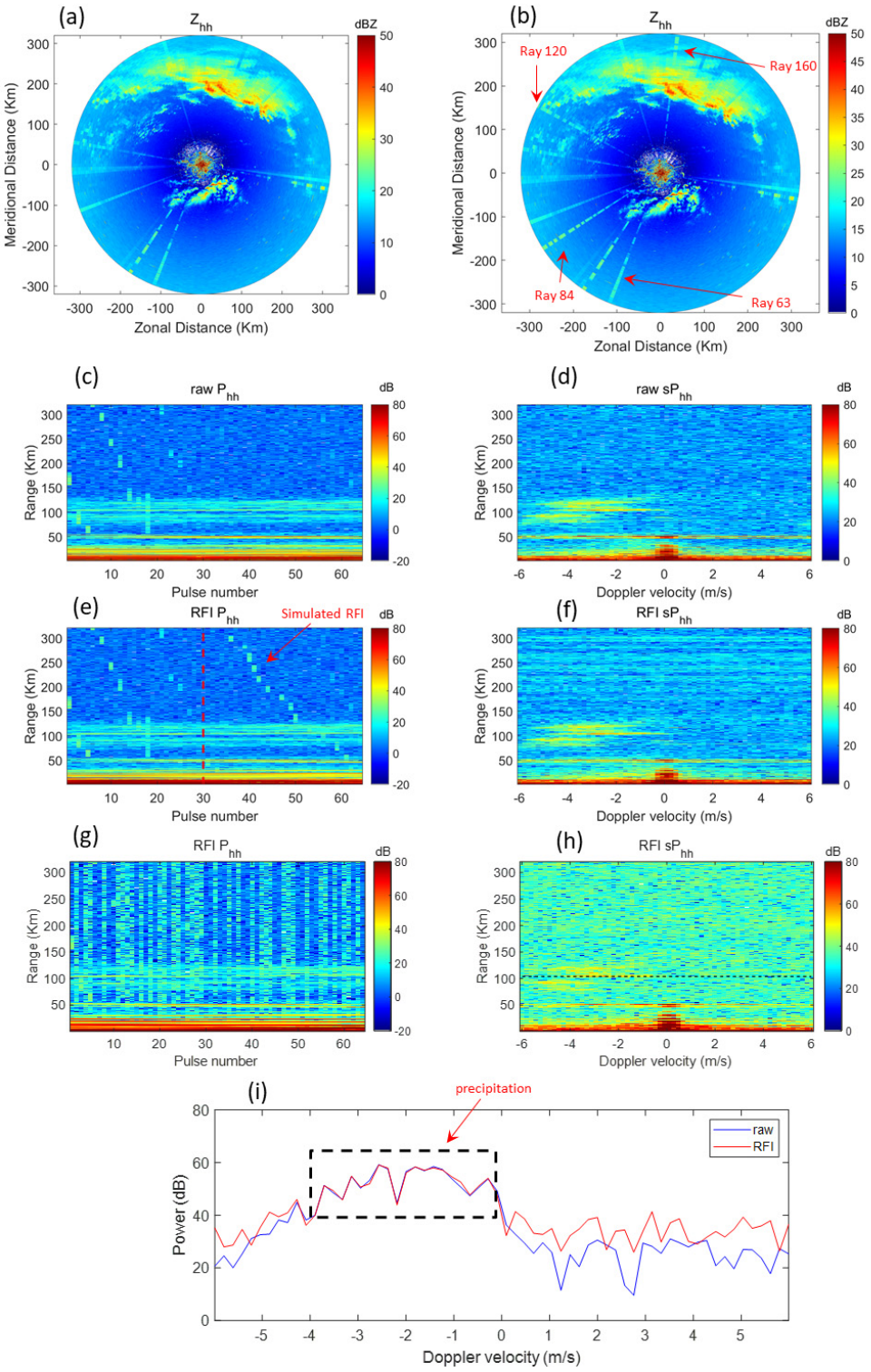

Fig. 5. Simulated RFI pulses with the maximum SNR 30 dB added to the KNMI Herwijnen radar data. (a) Raw reflectivity Z_{hh} PPI; (b) raw reflectivity Z_{hh} PPI with simulated RFI in Rays 84, 120 and 160; (c) range-time image of Ray 71; (d) range-Doppler spectrogram of Ray 71; (e) range-time image of Ray 71 with simulated RFI (maximum INR 11.9 dB and RFI contamination ratio of 2.7%); (f) range-Doppler spectrogram of Ray 71 with simulated RFI (maximum INR 11.9 dB and RFI contamination ratio of 2.7%); (g) range-time image of Ray 71 with simulated RFI (maximum INR 17.4 dB and RFI contamination ratio of 33.9%); (h) range-Doppler spectrogram of Ray 71 with the simulated RFI (maximum INR 17.4 dB and RFI contamination ratio of 33.9%); and (i) Doppler spectra of range 104 km with and without simulated RFI.

the three azimuth directions. Note that Ray 160 crosses the precipitation, which provides a good evaluation case for the filter.

The raw range-pulse image of Ray 71 is displayed in Fig. 5(c), and its corresponding range-Doppler spectrogram is shown in Fig. 5(d). In the simulation, the parameter l

related to RFI pulselength is set in the interval of [80, 240] (the total range bin number is 4015), while the RFI pulse repetition times T_{RFI} are set based on the severity of RFI contamination. For the situations when the RFI contamination is not severe, n is set in the interval of [1, 3], and m is set in the interval of [40, 120]. On the contrary, when the RFI contamination is severe, we have $n = 0$, and m is set in the interval of [5, 20]. Correspondingly, we have two RFI patterns whose RFI contamination ratios are 2.7% and 33.9%, and their range-pulse images and range-Doppler spectrograms are shown in Fig. 5(e)–(h).

When the RFI contamination ratio is small (2.7%), RFI pulses are added starting from pulse number 30 in Fig. 5(e). In that case, a similar RFI signature is observed in the time and spectral domains compared to the real KNMI measurements [e.g., Fig. 1(b) and (c)]. Moreover, when more bins in the range-pulse image are contaminated by RFI, the INR of RFI will increase, as shown in the background color changes in Fig. 5(d), (f), and (h). The noise level of the RFI-contaminated range gates is increased, masking weak precipitation (e.g., the boundary precipitation) or other weak clutter. Specifically, the maximum INRs of Fig. 5(f) and (h) are 11.9 and 17.4 dB, respectively.

Finally, the Doppler power spectra of range 104 km taken from Fig. 5(d) and (h), representing cases without and with RFI contamination, are displayed in Fig. 5(i). We can see that the whole noise floor is increased, which is consistent with literature [11]. However, those Doppler bins with large backscattered power remain the same, namely, the precipitation centered around $-2\ \mathrm{m\,s^{-1}}$. The increased noise (i.e., RFI) should be mitigated; otherwise, it will bias the radar observable estimation.

IV. OBSPol Filter and Its Applications

Recently, the OBSpol filter [13] was designed by the authors for narrowband clutter (i.e., ground clutter and moving artifacts) and noise mitigation. Based on the difference of spectral polarimetric features and range-Doppler continuity of precipitation and clutter, the filter has been proven effective, and its performance has been validated by several case studies. This filter can be very general, and in this article, it is analyzed for RFI mitigation. In this section, the OBSpol filter will be described briefly, and its applications to radar measurements are discussed.

A. Filter Description

The flowchart of the OBSpol filter is shown in Fig. 6. The filter is implemented in the range-Doppler domain such that the input is a raw spectrogram and the output is the filtered one. The OBSpol filter contains four steps. First, the spectral polarimetric observables are utilized to generate a binary mask where "1" indicates the precipitation (thresholding technique). In Step 2, the mathematical morphology method is used to recover the missing precipitation areas of the obtained mask. Based on the reconstructed mask in Step 2, the contiguous bins having values "1" are selected and integrated into several separate areas in the range-Doppler spectrogram termed

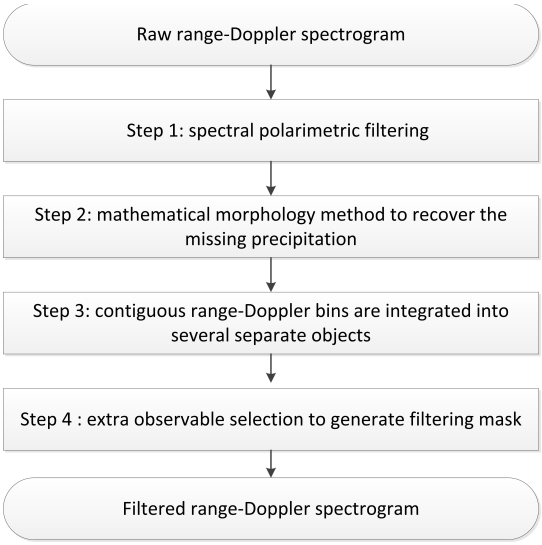

Fig. 6. Flowchart of the OBSpol filter applied to RFI mitigation.

"objects" in Step 3. Next, in Step 4, whether the produced objects are precipitation or not is further decided based on the appropriate observable. Thus, a filtering mask can be obtained by summing up the filtered separated objects.

It is recommended that a proper Doppler dealiasing technique is used before the implementation of the OBSpol filter. After the dealiasing technique, precipitation is integrated into a small number of objects. Note that the spectral polarimetric variables in Step 1 can be spectral linear depolarization ratio [24], spectral depolarization ratio [25], or $s\rho_{\mathrm{co}}$, leading to different versions of the OBSpol filters, which are applicable to polarimetric radar with (i.e., the AHV mode) and without cross-polar measurements (i.e., the SHV mode). As visualized in Fig. 3(e) and (g), the $s\rho_{\mathrm{co}}$ differences between precipitation and RFI become larger in the AHV mode.

Therefore, the pulse sequences of SHV radar can be divided into two subsequences [i.e., H_{2m-1} and V_{2m} and H_{2m} and V_{2m-1} from Fig. 2(a)]. Such division helps to decorrelate the RFI between two consecutive channels. Hereafter, for SHV radar, we refer to the conventional $s\rho_{\mathrm{co}}$ as SHV $s\rho_{\mathrm{co}}$ and the one derived from subsequences as AHV $s\rho_{\mathrm{co}}$. After using the OBSpol filter with AHV $s\rho_{\mathrm{co}}$, the subsequent results can be merged. In this article, the merging method is performed by the simple summation of two subspectrograms; a proper Doppler dealiasing method (e.g., [19]) remains for future work. The power-related variables, such as reflectivity and differential reflectivity, can be obtained after the filtering.

According to the spectral polarimetric variables studied in Section II C, the $s\rho_{\mathrm{co}}$ and sZ_{dr} filtering is utilized in Step 1. Specifically, range-Doppler bins with $s\rho_{\mathrm{co}}$ less than a threshold and sZ_{dr} outside of [−3 dB, 4 dB] are discarded. This spectral copolar correlation coefficient threshold is selected to keep rain. Specifically, as indicated in Fig. 3(e) and (g), after one SHV sequence is divided into two AHV sequences, the spectral copolar correlation coefficient of precipitation is decreased. Accordingly, the thresholds are chosen based on different sequence modes: 0.98 for the SHV mode and 0.90 for

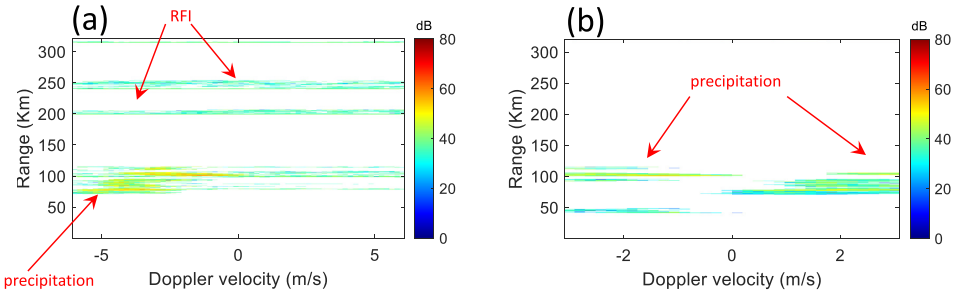

Fig. 7. KNMI Herwijnen radar spectrogram comparison. (a) OBSpol filter with SHV $s\rho_{\rm co}$. (b) OBSpol filter with AHV $s\rho_{\rm co}$.

the AHV mode. The thresholds can be decreased to keep as well drizzle and other hydrometeor types. In addition, a ground clutter suppression technique should be included due to the inability of the filter using both $s\rho_{\rm co}$ and $sZ_{\rm dr}$ to remove ground clutter. This ground clutter suppression consists of a notch filter around 0 m/s having a width of 1.12 m/s.

Step 4 of the OBSpol filter was designed to achieve narrowband clutter mitigation [13]. Based on the facts that: 1) RFI acts as noise with larger power in the range-Doppler spectrogram and 2) the OBSPol filter can remove the noise; it is expected that good RFI mitigation performance can be achieved by keeping the same Step 4. Namely, the spectral width acts as the extra observable, and its threshold is set to 10% of the Doppler bins number.

B. Application to Real and Simulated RFI Data

The data considered are the same as in Fig. 5. The radar configuration for acquiring the data has been described in Section II-A, and 64 samples of pulses are taken to generate the range-Doppler spectrogram. In the following, for the spectrograms and PPIs, we use the RFI pattern with the RFI contamination ratio of 33.9% but with different SNRs for the added pulses. This RFI contamination ratio is selected because this one is challenging for removing the RFI in the time domain, while the spectral domain offers mitigation possibilities.

The quantitative analysis of estimated radar variables is provided, and the metrics used are the mean bias error (MBE) and the root mean square error (RMSE). Supposing a given spectrogram, where we have R range bins with precipitation, the MBE and RMSE of a specific observable X can be expressed as

$$\mathrm{MBE}(X) = \frac{1}{R}\sum_{r=1}^{R}\left(X^{\rm est}(r) - X^{\rm tru}(r)\right) \tag{15}$$

$$\mathrm{RMSE}(X) = \sqrt{\frac{1}{R}\sum_{r=1}^{R}\left(X^{\rm est}(r) - X^{\rm tru}(r)\right)^2} \tag{16}$$

where $X^{\rm tru}(r)$ is the true observable value in the rth range bin, which is manually selected, and $X^{\rm est}(r)$ is the filtered observable value in the rth range bin. Note that the observable X can be reflectivity Z_{hh} or differential reflectivity $Z_{\rm dr}$.

In the spectrograms, the ground-truth areas of precipitation are manually selected. The manual selection yields a binary mask where "1" represents precipitation. The selection is based on three criteria: 1) the range-Doppler continuity of precipitation; 2) spectral SNR thresholding; and 3) spectral polarimetric values ($s\rho_{\rm co}$) thresholding. Specifically, any bin in the range-Doppler spectrogram with a spectral power less than the estimated noise will be removed; any bin with a $s\rho_{\rm co}$ value smaller than the set threshold will be discarded. These thresholds are obtained from the clutter and precipitation spectral polarimetric value distributions. In addition, the precipitation should be continuous in the range-Doppler spectrogram. By using image processing techniques (i.e., the mathematical morphology), some of the zeros inside the precipitation mask are filled.

1) Spectrograms: First, the filter applied to the spectrograms is checked. Ray 70 with real RFI is taken, and the original sP_{hh} spectrogram is displayed in Figs. 1(c) (in the SHV mode) and 3(f) (in the AHV mode). The corresponding filtered spectrograms using the OBSpol filter are shown in Fig. 7. The OBSPol filter with SHV $s\rho_{\rm co}$ can only preserve precipitation with large SNR but also retains more residual RFI, which is not the case of the OBSPol filter with AHV $s\rho_{\rm co}$. When filtered spectrograms derived from both H_{2m-1} and V_{2m}, and H_{2m} and V_{2m-1} are combined, which is equivalent to the full number of samples, precipitation without RFI contamination can be obtained. Currently, the Doppler aliasing problem due to the selected half samples is not solved yet. Thus, we will quantify the filtering performance in PPI in terms of power-related variables (e.g., Z_{hh} and $Z_{\rm dr}$).

Considering another ray (Ray 160) and keeping the RFI contamination ratio of 33.9% (see Fig. 5(g) for the pattern), RFI pulses with the INR of 18.6 dB are added to the raw measurements. The raw spectrogram and the RFI contaminated one are shown in Fig. 8(a) and (b). Then, the OBSpol filter with SHV $s\rho_{\rm co}$ and AHV $s\rho_{\rm co}$ is applied to the contaminated sP_{hh}, and their corresponding results are displayed in Fig. 8(c) and (d). It is obvious that the filter with AHV $s\rho_{\rm co}$ has a better performance in RFI removal. Note that the filters are unable to recover weather signals beyond 240 km because precipitation is buried by RFI in the spectral domain, as indicated by the comparison between Fig. 8(a) and (b). For better visualizing the performance of different processing, the Z_{hh} and $Z_{\rm dr}$ scatterplots of true values and estimated values are displayed in Fig. 8(e)–(j). Note that "contaminated" in Fig. 8(e) and (f) means that the variables are calculated by using data located in the true precipitation areas but contaminated by the addition of RFI.

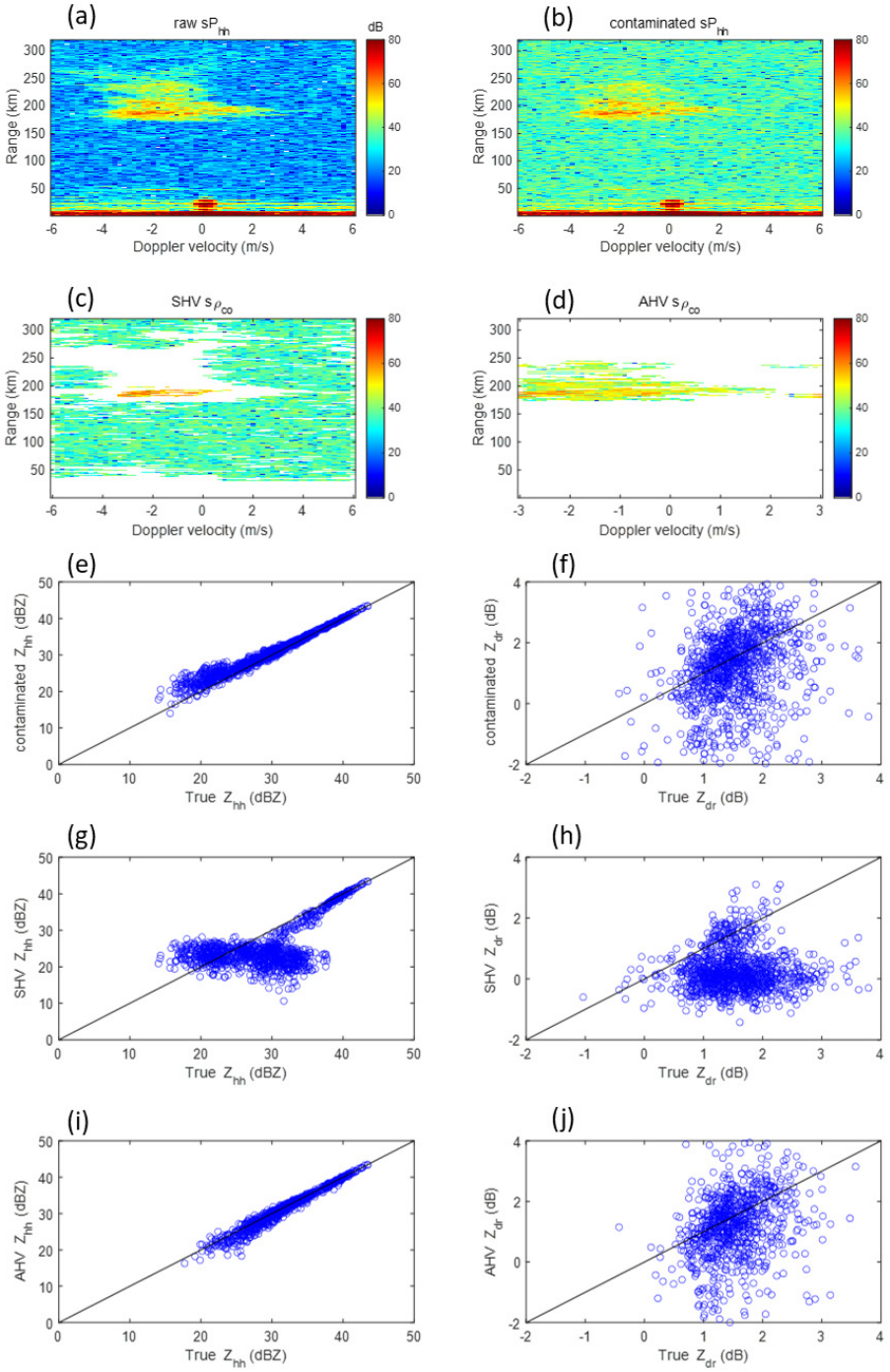

Fig. 8. Performance comparison between the SHV $s\rho_{\rm co}$ and the AHV $s\rho_{\rm co}$ used in the OBSpol filter. (a) Raw spectrogram; (b) spectrogram with INR 18.6 dB; (c) spectrogram filtered by the OBSpol with SHV $s\rho_{\rm co}$; (d) spectrogram filtered by the OBSpol with AHV $s\rho_{\rm co}$; (e) scatterplot between the true Z_{hh} and the RFI-contaminated Z_{hh}; (f) scatterplot between the true $Z_{\rm dr}$ and the RFI-contaminated $Z_{\rm dr}$; (g) scatterplot between the true Z_{hh} and SHV Z_{hh}; (h) scatterplot between the true $Z_{\rm dr}$ and SHV $Z_{\rm dr}$; (i) scatterplot between the true Z_{hh} and AHV Z_{hh}; and (j) scatterplot between the true $Z_{\rm dr}$ and AHV $Z_{\rm dr}$.

For this specific case, the results from the OBSpol with SHV $s\rho_{\rm co}$ have the largest MBE for both Z_{hh} (-3.68 dBZ) and $Z_{\rm dr}$ (-1.28 dB). While the OBSpol with AHV $s\rho_{\rm co}$ performs the best, the Z_{hh} MBE is -0.48 dBZ, and the $Z_{\rm dr}$ MBE is -0.33 dB. Moreover, the OBSpol with AHV $s\rho_{\rm co}$ has also the smallest RMSE values of Z_{hh} (1.05 dBZ) and $Z_{\rm dr}$ (1.14 dB).

To quantify the impact of the added pulses SNR on the filtering performance, a simulation is performed where the same RFI pattern of Fig. 5(g) is used, but the maximum SNR is set to be different (ranging from 5 to 25 dB). The corresponding MBE and RMSE of Z_{hh} and $Z_{\rm dr}$ are displayed versus INR in Fig. 9. With the increase in INR, the estimated observables deviate more from the ground truth. Overall, the OBSpol with AHV $s\rho_{\rm co}$ performs the best.

To further evaluate the performance of the filters, two precipitation cases are chosen. Five consecutive rays of each

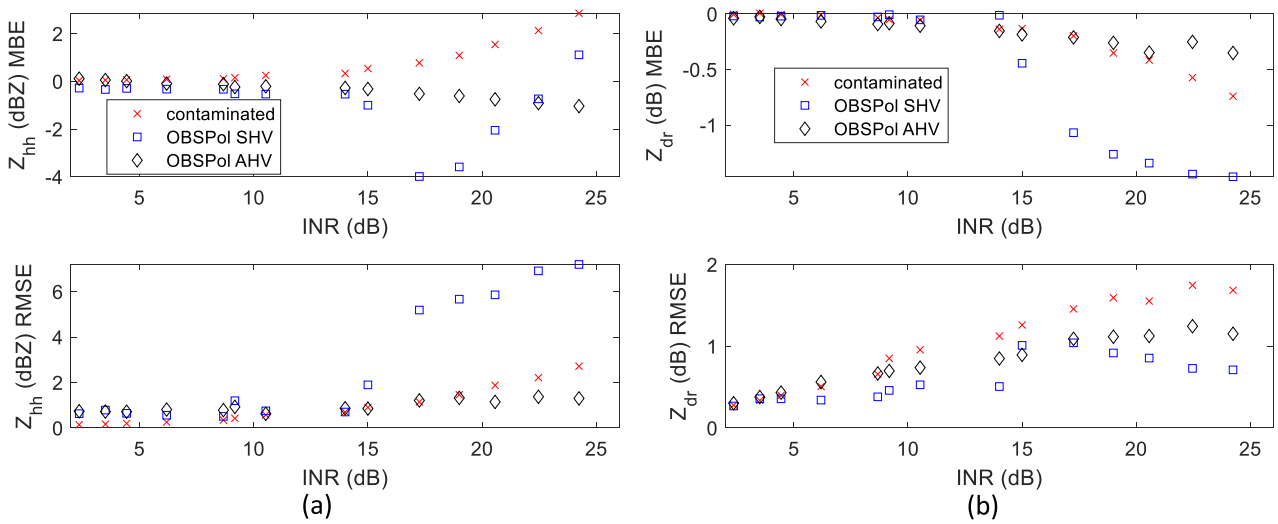

Fig. 9. MBE and RMSE of radar observables versus INR. (a) Z_{hh}. (b) Z_{dr}. The INR values relate to the SNR of the added RFI pulses, and the RFI contamination ratio is 33.9%.

TABLE III
MBE AND RMSE OF RADAR OBSERVABLES

Case No.	Ray No.	MBE						RMSE					
		contaminated		OBSPol SHV		OBSPol AHV		contaminated		OBSPol SHV		OBSPol AHV	
		Z_{hh}	Z_{dr}	Z_{hh}	Z_{dr}	Z_{hh}	Z_{dr}	Z_{hh}	Z_{dr}	Z_{hh}	Z_{dr}	Z_{hh}	Z_{dr}
1	160	0.75	-0.25	-4.21	-1.09	-0.40	-0.14	1.12	1.37	5.42	1.08	1.00	0.96
	161	1.86	-0.53	-1.76	-1.48	-0.34	-0.26	2.07	1.60	6.10	0.80	1.27	1.14
	162	0.60	-0.20	-4.58	-1.04	-0.23	-0.18	0.91	1.32	4.33	1.14	0.84	1.13
	163	1.19	-0.45	-3.12	-1.33	-0.47	-0.23	1.48	1.55	5.47	1.05	1.10	1.11
	164	0.58	-0.20	-3.15	-0.81	-0.35	-0.13	0.99	1.39	4.70	1.17	0.95	0.97
2	78	0.95	-0.36	-3.52	-0.74	-0.14	-0.30	1.44	1.27	4.66	1.08	1.34	0.96
	79	2.47	-0.64	-0.52	-1.39	-0.40	-0.25	2.52	1.60	6.41	0.87	0.97	0.92
	80	2.23	-0.55	-0.73	-1.49	-0.60	-0.19	2.25	1.70	7.28	0.91	1.07	1.09
	81	0.93	-0.41	-5.67	-1.32	-0.48	-0.24	1.30	1.60	6.72	0.98	1.21	1.19
	82	0.73	-0.25	-5.28	-1.05	-0.64	-0.28	1.11	1.54	5.24	1.18	1.25	1.15
average		1.23	-0.39	-3.25	-1.17	**-0.44**	**-0.24**	1.53	1.49	5.56	**1.01**	**1.14**	1.07

case in which clutter and precipitation do not overlap in the spectral domain and are free of Doppler aliasing are selected. For these data, the true precipitation is manually selected in the range-Doppler spectrogram, and we add pulses with the maximum INR 21.2 dB. The MBE and RMSE results are shown in Table III. On the one hand, for the MBE comparison, the OBSpol with AHV $s\rho_{\mathrm{co}}$ has the smallest values, and the average MBEs on Z_{hh} and Z_{dr} are -0.44 dBZ and -0.24 dB, respectively, while the OBSpol with SHV $s\rho_{\mathrm{co}}$ performs the worst. A negative MBE in Z_{hh} indicates that weak precipitation is removed, while a positive MBE relates to keeping RFI contamination. In the case of OBSpol with SHV $s\rho_{\mathrm{co}}$, not only weak precipitation may be discarded but also precipitation with sufficient SNR. This relates to the selection of a too high threshold for $s\rho_{\mathrm{co}}$ of 0.98, instead of 0.90 in the case OBSpol AHV $s\rho_{\mathrm{co}}$ to significantly suppress the high correlated RFI.

For Z_{dr}, the MBE is negative, which corresponds to our choice of an RFI with polarization 45° in the simulation. On the other hand, for the metric of RMSE, the OBSpol with AHV $s\rho_{\mathrm{co}}$ has the smallest value (1.14 dBZ), followed by the RFI contaminated one (1.53 dBZ), and then the OBSpol with SHV $s\rho_{\mathrm{co}}$ (5.56 dBZ). As for the Z_{dr} RMSE values, the OBSpol with SHV $s\rho_{\mathrm{co}}$ has the smallest value, being 1.01 dB. The reason might be that the remaining noise-like RFI dominates and decreases the Z_{dr} RMSE value.

2) PPIs: The original and filtered PPIs of Z_{hh} and Z_{dr} in both SHV and AHV modes are shown in Fig. 10. To explore the influence of the RFI polarization on filter performance, the simulated RFI is modeled as to be differently polarized, and we add pulses with the maximum SNR of 30 dB. Specifically, the simulated RFI linear polarization ranges from 5° to 45° with a step of 5°. The different polarized RFIs are added from Ray 60 to Ray 220 with a ray step of 20. As observed in Fig. 10(b), Rays 140, 160, and 180 are close to the real measurements, while the rest has some deviation.

Both filters can keep most of the precipitation and mitigate some RFI. Compared with the OBSpol filter with SHV $s\rho_{\mathrm{co}}$, the filter with AHV $s\rho_{\mathrm{co}}$ has a better performance in RFI mitigation, real and simulated, essentially because of the decorrelation of the RFI signal HH and VV in the AHV case. In this case, the OBSpol filter with SHV $s\rho_{\mathrm{co}}$ can mitigate all the RFI whose INR is less than 10 dB, namely, the real RFI, since the simulated one has the maximum SNR of 30 dB, while the one with AHV $s\rho_{\mathrm{co}}$ can remove almost all the RFI. In addition, noise is mitigated in both filters. This spectral

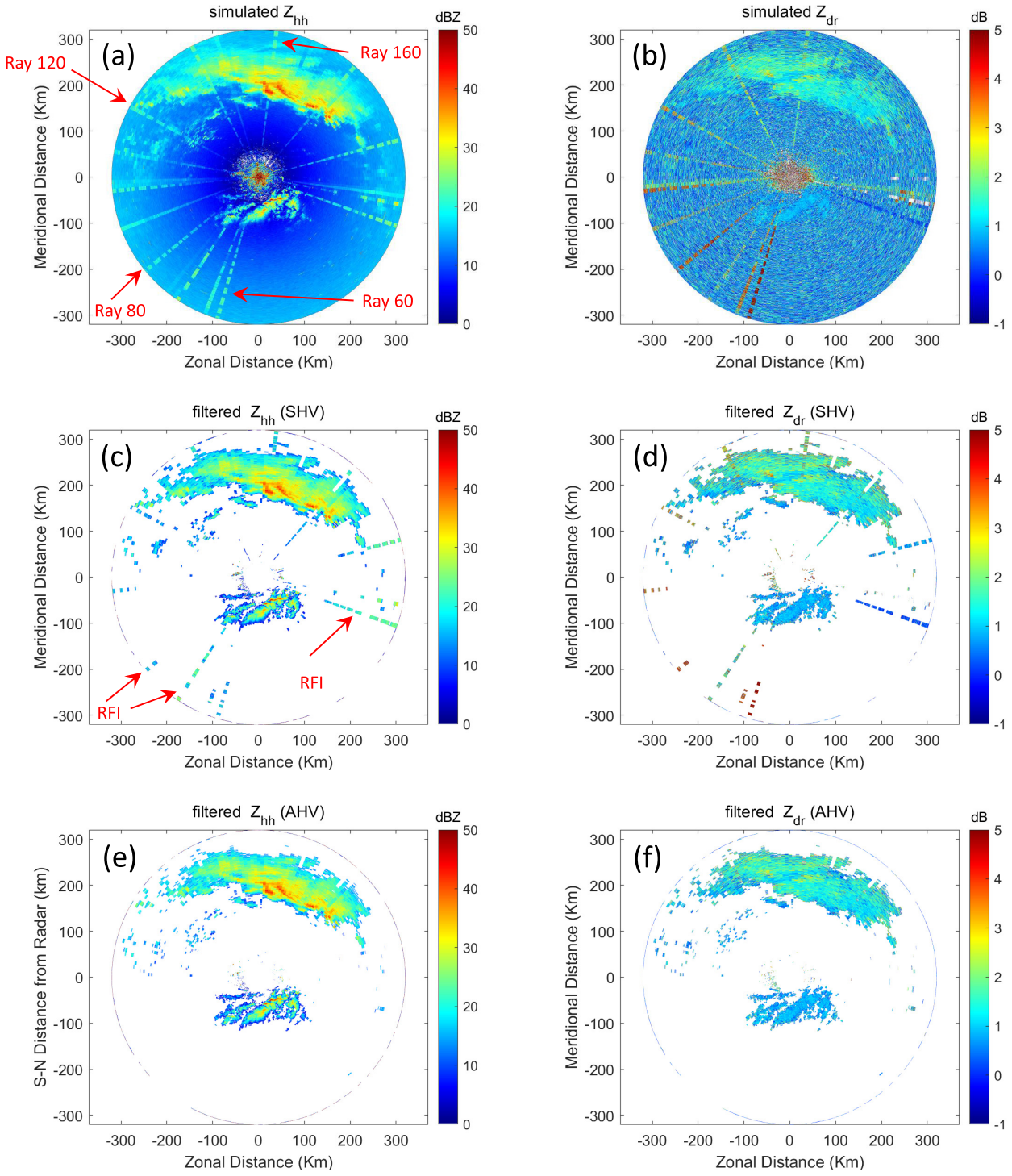

Fig. 10. KNMI Herwijnen radar PPIs comparison. Note that Rays 60–220 with a ray step of 20 are added with simualted RFI with maimum SNR of 30 dB. Those simulated RFI have different linear polarization, ranging from 5° to 45° with a step of 5°. (a) Raw Z_{hh}; (b) raw Z_{dr}; (c) filtered Z_{hh} by using OBSpol with SHV $s\rho_{\mathrm{co}}$; (d) filtered Z_{dr} by using OBSpol with SHV $s\rho_{\mathrm{co}}$; (e) filtered Z_{hh} by using OBSpol with AHV $s\rho_{\mathrm{co}}$; and (f) filtered Z_{dr} by using OBSpol with AHV $s\rho_{\mathrm{co}}$.

polarimetric filter can improve not only the observation [e.g., the weak precipitation at short range in Fig. 10(d) and (f), which is masked in the neighboring background in Fig. 10(b)] but also the radar observable quality [e.g., the precipitation overlapping with RFI in Fig. 10(b)].

Based on Table III, we expect significant errors on the reflectivity filtered with OBSpol SHV $s\rho_{\mathrm{co}}$ when the INR is large. Therefore, OBSpol AHV $s\rho_{\mathrm{co}}$ can improve the reflectivity estimation in that case. It improves as well Z_{dr}. However, considering the MBE and RMSE of Table III, the differential reflectivity will be contaminated by RFI in the case of large INR.

The processing time for Fig. 10(c) and (d) generation is 46.1 s by using MATLAB 2016b in a Windows 7 desktop PC

with a 3.6-GHz Intel Xeon E5-1620 CPU and 16-GB RAM, while the time elapsed for Fig. 10(e) and (f) generation is 69.6 s. According to the time statistical analysis, Step 3 of the OBSpol filter is the most time-consuming step. In addition, implementing the AHV mode processing twice requires more time than that of the SHV mode processing once.

V. Conclusion

RFI has become a growing concern for weather radar. Aiming at mitigating RFI for polarimetric weather radar, one spectral polarimetric filter named the OBSPol filter is used in this article. In this research, the real RFI measurements from operational C-band weather radar, KNMI Herwijnen radar, are used to characterize the RFI type RLAN temporal, spectral, and polarimetric features. On the one hand, RFI in polarimetric radar can be regarded as raised noise in the spectral domain for each channel (also applied to single-polarization radar). On the other hand, considering the correlation between two channels, different polarimetric radar types have different impacts. For SHV radar, the RFI sensed by the horizontal and vertical channels will be correlated, while, for AHV radar, RFI detected by the two consecutive channels will be uncorrelated.

Based on these features, the RFI type RLAN is simulated to investigate the performances of the OBSPol filter. This filter is multifunctional for mitigating different types of clutter. Specifically, initially designed for removing narrowband clutter (i.e., moving artifacts and ground clutter) and noise, the OBSpol filter is analyzed for the application of RFI mitigation. Based on the spectral polarimetric features and range-Doppler continuity of precipitation, the filter generates a filtering mask implemented on the raw range-Doppler spectrogram to retain the precipitation and remove the clutter. Overall, the OBSpol filter suppresses clutter well while preserving weak precipitation when clutter and precipitation are separable in the spectral domain [13].

In challenging contamination (high RFI contamination ratio) in the time domain, the spectral domain offers perspectives in the RFI mitigation, in particular when precipitation and RFI overlap in the time domain.

Due to the high correlation between HH and VV RFI measurements in SHV radar, generation of the AHV $s\rho_{\mathrm{co}}$ as a replacement of SHV $s\rho_{\mathrm{co}}$ is suggested for the filter design in RFI mitigation. The Doppler dealiasing technique [19] specific for the AHV mode, which allows the recovery of the SHV maximum unambiguous Doppler velocity, should be implemented next. Furthermore, the simple RFI model proposed may be extended in the future after analyzing a large database of RFI signatures.

The OBSpol filter is applicable with different Doppler velocity resolutions [13]. It is worth mentioning that the OBSpol filter has been applied to an operational C-band radar with pulse number 64 in this work, and good clutter mitigation performance is achieved. The OBSpol filter is implemented in the spectral domain, in which the precipitation is concentrated in a limited quantity of Doppler bins, whereas the RFI is evenly spread. However, if the power level of precipitation does not stand out above the "noise plus interference" level, then the filter cannot distinguish precipitation from the raised "noise," resulting in some precipitation loss.

The OBSpol filter cannot resolve the problem when clutter is embedded into the precipitation in the spectral domain. Such a problem was recently investigated by proposing a method that combines clutter-contaminated precipitation identification and recovery using spectral polarimetric features and kriging [26]. How to adapt the designed method to the situation of precipitation overlapping with RFI should be a focus of future research.

Furthermore, this work built a typical RFI model based on operational C-band radar measurements, which is also verified by published literature, such as [3], [5], and [11]. This research work considers the situation where RFI is linearly polarized. However, the polarimetric features of circular and 45° linear polarized RFI are similar. Therefore, we expect the same performance in terms of filtering results. Since there is an increasing number of RF devices, a throughout RFI characterization experiment is necessary to quantify the RF sources in a controlled manner. Correspondingly, the impact of RFI with different polarization can be quantified by real measurements.

Moreover, the focus of this work is not a full evaluation of the RFI mitigation performance on all radar data outputs but a proof of concept to show the effectiveness of the proposed filter for RFI mitigation. The first assessment of the reflectivity and differential reflectivity statistics has been made. Next, other radar products, such as the Doppler spectrum width, the copolar correlation coefficient, and the differential phase, should be evaluated as well. In addition, more data collected in different meteorological conditions (i.e., both during summer and winter) should be used for a complete assessment of the RFI filter.

Acknowledgment

The authors would like to thank John Y. N. Cho from the Massachusetts Institute of Technology for his discussion on the topic of radio frequency interference. They would like to thank Hidde Leijnse and Tiemo Mathijssen for providing the KNMI radar data.

References

[1] V. N. Bringi and V. Chandrasekar, *Polarimetric Doppler Weather Radar: Principles and Applications*. Cambridge, U.K.: Cambridge Univ. Press, 2001.

[2] J. Yin, P. Hoogeboom, C. Unal, H. Russchenberg, F. van der Zwan, and E. Oudejans, "UAV-aided weather radar calibration," *IEEE Trans. Geosci. Remote Sens.*, vol. 57, no. 12, pp. 10362–10375, Dec. 2019.

[3] J. Y. N. Cho, "A new radio frequency interference filter for weather radars," *J. Atmos. Ocean. Technol.*, vol. 34, no. 7, pp. 1393–1406, Jul. 2017.

[4] *Use of the Bands 5150-5250 MHz, 5250-5350 MHz and 5470-5725 MHz by the Mobile Service for the Implementation of Wireless Access Systems Including Radio Local Area Networks*, document ITU-R Resolution 229, 2003.

[5] M. Vaccarono, V. Chandrasekar, R. Bechini, and R. Cremonini, "Survey on electromagnetic interference in weather radars in northwestern Italy," *Environments*, vol. 6, no. 12, p. 126, 2019.

[6] P. Tristant, "RLAN 5 GHz interference to C-band meteorological radars in Europe: Solutions, lessons, follow-up," in *Proc. 34th AMS Radar Conf. Radar Meteorol.*, 2009.

[7] J. E. Carroll, F. H. Sanders, R. L. Sole, and G. A. Sanders, "Case study: Investigation of interference into 5 GHZ weather radars from unlicensed national information infrastructure devices," U.S. Dept. Commerce, Nat. Telecommun. Inf. Admin., Washington, DC, USA, Tech. Rep., 2010.

[8] E. Saltikoff *et al.*, "The threat to weather radars by wireless technology," *Bull. Amer. Meteorol. Soc.*, vol. 97, no. 7, pp. 1159–1167, 2016.

[9] J. Lake, M. Yeary, and C. Curtis, "Adaptive radio frequency interference mitigation techniques at the national weather radar testbed: First results," in *Proc. IEEE Radar Conf.*, May 2014, pp. 840–845.

[10] Vaisala. (2016). *User's Manual: RVP900 Digital Receiver and Signal Processor*. [Online]. Available: ftp://ftp.sigmet.com/outgoing/manuals/RVP900_Users_Manual.pdf

[11] P. Joe, J. Scott, J. Sydor, A. Brandão, and A. Yongacoglu, "Radio local area network (RLAN) and C-band weather radar interference studies," in *Proc. 32nd AMS Radar Conf. Radar Meteorol.*, 2005.

[12] L. Rojas, D. N. Moisseev, V. Chandrasekar, J. Sezler, and R. Keränen, "Dual-polarization spectral filter for radio frequency interference suppression," in *Proc. Eur. Conf. Radar Meteorol. Hydrol. (ERAD)*, 2012.

[13] J. Yin, C. Unal, and H. Russchenberg, "Object-orientated filter design in spectral domain for polarimetric weather radar," *IEEE Trans. Geosci. Remote Sens.*, vol. 57, no. 5, pp. 2725–2740, May 2019.

[14] A. Huuskonen, E. Saltikoff, and I. Holleman, "The operational weather radar network in Europe," *Bull. Amer. Meteorol. Soc.*, vol. 95, no. 6, pp. 897–907, 2014.

[15] (May 2021). *Precipitation Map From KNMI Weather Radars*. [Online]. Available: https://www.buienradar.nl/

[16] (May 2021). *KNMI Data*. [Online]. Available: https://data.knmi.nl/datasets/

[17] V. M. Melnikov and D. S. Zrnić, "On the alternate transmission mode for polarimetric phased array weather radar," *J. Atmos. Ocean. Technol.*, vol. 32, no. 2, pp. 220–233, 2015.

[18] B. Y. Toh, R. Cahill, and V. F. Fusco, "Understanding and measuring circular polarization," *IEEE Trans. Educ.*, vol. 46, no. 3, pp. 313–318, Aug. 2015.

[19] C. M. H. Unal and D. N. Moisseev, "Combined Doppler and polarimetric radar measurements: Correction for spectrum aliasing and nonsimultaneous polarimetric measurements," *J. Atmos. Ocean. Technol.*, vol. 21, no. 3, pp. 443–456, Mar. 2004.

[20] F. J. Meyer, J. B. Nicoll, and A. P. Doulgeris, "Correction and characterization of radio frequency interference signatures in L-band synthetic aperture radar data," *IEEE Trans. Geosci. Remote Sens.*, vol. 51, no. 10, pp. 4961–4972, Oct. 2013.

[21] I. R. Ivić, C. Curtis, and S. M. Torres, "Radial-based noise power estimation for weather radars," *J. Atmos. Ocean. Technol.*, vol. 30, no. 12, pp. 2737–2753, Dec. 2013.

[22] S. Bachmann and D. Zrnić, "Spectral density of polarimetric variables separating biological scatterers in the VAD display," *J. Atmos. Ocean. Technol.*, vol. 24, no. 7, pp. 1186–1198, Jul. 2007.

[23] D. N. Moisseev and V. Chandrasekar, "Polarimetric spectral filter for adaptive clutter and noise suppression," *J. Atmos. Ocean. Technol.*, vol. 26, no. 2, pp. 215–228, Feb. 2009.

[24] J. Yin, C. M. H. Unal, and H. W. J. Russchenberg, "Narrow-band clutter mitigation in spectral polarimetric weather radar," *IEEE Trans. Geosci. Remote Sens.*, vol. 55, no. 8, pp. 4655–4667, Aug. 2017.

[25] J. Yin, H. Chen, Y. Li, and X. Wang, "Clutter mitigation based on spectral depolarization ratio for dual-polarization weather radars," *IEEE J. Sel. Topics Appl. Earth Observ. Remote Sens.*, vol. 14, pp. 6131–6145, Jun. 2021.

[26] J. Yin, M. Schleiss, and X. Wang, "Clutter-contaminated signal recovery in spectral domain for polarimetric weather radar," *IEEE Geosci. Remote Sens. Lett.*, early access, Mar. 12, 2021, doi: 10.1109/LGRS.2021.3063355.

Jiapeng Yin received the B.Sc. degree in information engineering from the National University of Defense Technology (NUDT), Changsha, China, in 2012, and the Ph.D. degree in atmospheric remote sensing from the Delft University of Technology, Delft, The Netherlands, in 2019.

He is an Assistant Professor with the College of Electronic Science, NUDT. His research interests include radar polarimetry, polarimetric weather radar, radar signal processing, and radar calibration.

Peter Hoogeboom received the M.S.E. degree in electrical engineering from the Delft University of Technology (TU Delft), Delft, The Netherlands, in 1975.

He worked for more than 40 years in radar remote sensing and instruments. He held several research and management positions. For over ten years, he managed research groups on radar and remote sensing at TNO, an organization for applied physics research in Hague, The Netherlands. Since 1999, he has been a Professor of radar and earth observation with the Delft University of Technology, where he has been involved in instrument studies, calibration, and applications of radars for remote sensing, including atmospheric radar. After his retirement in 2017, he continued part-time work with the Geoscience and Remote Sensing Department, TU Delft, where his experience contributes to a wide range of studies on atmospheric and earth applications of radar.

Christine Unal received the master's degree in physics from the University of Nice Sophia Antipolis, Nice, France, in 1986, and the D.E.A. degree in physics for remote sensing from the University of Paris, Paris, France, in 1987.

She joined the Delft University of Technology, Delft, The Netherlands, in 1988, where she is a Research Scientist. She was first at the International Research Center for Telecommunications and Radar, Delft University of Technology. Since 2012, she has been with the Department of Geoscience and Remote Sensing and the Climate Institute, Delft University of Technology. She started to focus on radar polarimetric calibration and radar spectral polarimetry (quasi-simultaneous Doppler spectra of polarimetric measurements, their processing, and their interpretation). Since 2003, she has been applying this expertise to enhance the processing of atmospheric echoes. Since 2012, her research interests are weather/atmospheric radar signal processing and searching for new retrieval techniques to estimate microphysical and dynamical properties of precipitation using ground-based radars.

Herman Russchenberg is the Director of the Climate Institute, Delft University of Technology (TU Delft), Delft, The Netherlands, where he is also the Head of the Department of Geoscience and Remote Sensing. He is one of the leading scientists of the Cabauw Experimental Site for Atmospheric Research. He is a specialist in remote sensing of clouds and precipitation with ground-based radar, LiDAR, and microwave radiometry. He is experienced in theoretical and experimental research of the scattering process and the retrieval of geophysical parameters from radar and LiDAR measurements.